



pubs.acs.org/acsaenm Article

Sulfonation-Induced Cross-Linking and Nanostructural Evolution of a Thermoplastic Elastomer for Ordered Mesoporous Carbon Synthesis: A Mechanistic Study

Mark Robertson, Andrew Barbour, Anthony Griffin, Alejandro Guillen Obando, Paul Smith, and Zhe Qiang*



Cite This: https://doi.org/10.1021/acsaenm.3c00359



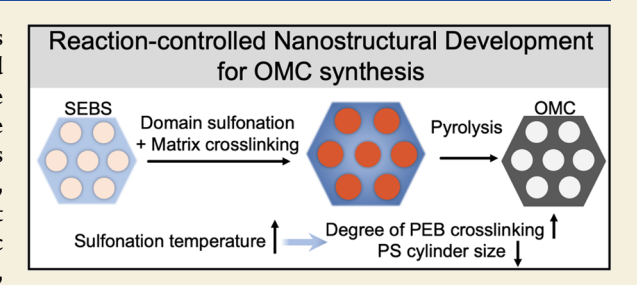
ACCESS I

III Metrics & More

Article Recommendations

s Supporting Information

ABSTRACT: Direct pyrolysis of self-assembled block copolymers (BCPs) is a resource-efficient method for synthesizing ordered mesoporous carbons (OMCs), through which the resulting pore textures and properties are often collectively determined by the precursor identity and processing pathways. Previous works in this area heavily rely on the use of polyacrylonitrile-based BCP systems, which employ a high-temperature cross-linking reaction that can impact the degree of ordering in their nanostructures. Recently, thermoplastic elastomers have been employed as an emerging OMC precursor, demonstrated by commodity grade polystyrene-block-poly(ethylene-ran-



butylene)-block-polystyrene (SEBS). This method requires solid-state, sulfonation-induced cross-linking, involving simultaneous reactions with both the majority poly(ethylene-ran-butylene) phase and the polystyrene segments. This work elucidates the fundamentals of how the reaction mechanism and condition govern SEBS nanostructure development, which deconvolutes distinct contributions from sulfonation and cross-linking. Specifically, small-angle X-ray scattering results, in conjunction with chemical evolution investigations, indicate that polystyrene sulfonation is primarily responsible for increased domain spacing that is mediated through competition between thermodynamically driven nanostructure rearrangement and kinetic trapping from cross-linking. The conversion of cross-linked SEBS, obtained from varying reaction conditions, to OMCs is also studied for establishing critical process—structure relationship. These fundamental understandings provide key insights about rational system design of SEBS-derived OMCs, prepared through two steps of sulfonation-induced cross-linking and direct pyrolysis.

KEYWORDS: block copolymer, self-assembly, reaction-induced morphology control, in situ SAXS, porous materials

■ INTRODUCTION

The synthesis of ordered mesoporous carbons (OMCs, pore size of 2-50 nm) has broadly enabled key advancement across many nanotechnology applications, including energy storage, environmental remediation, and catalysis, due to their advantages of relatively large surface areas and a long-range degree of ordering, which greatly facilitate mass transport and sorption of guest molecules into the carbon matrix. 1-5 Traditionally, OMCs have been synthesized using softtemplating methods that involve the cooperative assembly of an amphiphilic polymer template with a phenolic resin that acts as the precursor for the carbon matrix.^{6,7} This softtemplating approach can be employed to synthesize OMCs with tunable pore textures but requires multiple fabrication steps and large amounts of volatile solvent consumption for evaporation-induced self-assembly of the multicomponent solution after efficient mixing.8 As an alternative approach, direct pyrolysis of block copolymers (BCPs) has been demonstrated as a simplified and more resource-efficient method. 9,10 Typically, these BCPs contain a carbon-yielding

majority block, such as polyacrylonitrile (PAN), and a thermally labile block to form pores upon carbonization.
Synthesizing these BCP materials often requires multiple steps of reaction and purification, which can be time-consuming and costly. Additionally, in PAN-derived systems, the cross-linking reaction is typically performed above 200 °C and coincides with enhanced mobility and decreased χ values of the polymer constituents.
Consequently, reduced nanostructural ordering is imparted into the pore structure of the final OMC products with a feature of relatively broad pore size distributions.

Recently, synthesis of OMCs from thermoplastic elastomer (TPE) precursors has been demonstrated as an emerging route, using multiple different types of polystyrene-block-

Received: June 30, 2023
Revised: September 6, 2023
Accepted: September 8, 2023



poly(ethylene-ran-butylene)-block-polystyrene (SEBS) as model systems.¹⁷ Leveraging a sulfonation-induced crosslinking reaction, during which SEBS powders are submerged in concentrated sulfuric acid at increased temperatures, the olefinic poly(ethylene-ran-butylene) (PEB) matrix could be selectively cross-linked. Through a following step of direct pyrolysis, the PEB segment produces carbon, while the polystyrene (PS) block can be thermally decomposed to form pores, yielding the resulting OMC products. Notably, it was found that the sulfonation reaction can lead to simultaneous PS sulfonation and olefinic cross-linking, which can have a major impact on the nanostructure development of SEBS precursors. Interestingly, SEBS precursors with smaller volume fractions of PS exhibited significantly reduced domain swelling when comparing the neat polymer to the carbonized material, indicating the role of the PS sulfonation reaction in controlling the nanostructural rearrangement of the precursor.

The impact of low-temperature sulfonation reactions on TPE nanostructures was previously investigated by many groups due to their extensive use for membrane applications. 18-20 In these works, the reactions were typically performed in the solution state and only selectively functionalized PS segments. For example, Weiss et al. determined selective functionalization of PS minority phases in TPEs can result in significantly altered morphologies depending on the precursor nanostructure, degree of sulfonation, and counterion identity. 21-25 These factors all influence the TPE self-assembly behaviors, resulting in departure from the conventional BCP phase diagram, reduced order, and altered domain sizes, as well as increased order-to-disorder transition temperatures, which has been further supported and/or investigated by several other studies. 26-28 Mauritz et al. demonstrated that solutionstate sulfonation of SEBS resulted in nanostructural transitions from a hexagonally packed cylindrical morphology in the neat polymer to worm-like or lamellar morphologies depending on the degree of sulfonation of the PS minority phase. While the effects of the solution-state functionalization on SEBS morphologies have been investigated, the solid-state sulfonation introduces additional complexity through reactions at all blocks and restricted mobility in the bulk, especially when cross-linking of the olefinic matrix occurs. Specifically, during the reaction, the nanostructural rearrangement of SEBS occurs while the polymer precursor stays in the ordered morphology (potentially involving order-to-order transitions). Currently, the interplay between these competing phenomena, including structural rearrangement and kinetic trapping from chemical cross-linking, and their impact on the morphology development of the polymer and derived OMC products remain unclear. Understanding processing pathway-structure relationships of BCP self-assembly is important and necessary, 29,30 which can inform rational system design with reproducible pore structure control for OMC synthesis. 31,32

This work systematically investigates effects of simultaneous sulfonation and cross-linking reactions on the nanostructure development of a SEBS precursor, to understand their respective impact; multiple different reaction conditions are used to deconvolute the impact from sulfonation and cross-linking. In particular, the chemical transformation of the SEBS precursors at different reaction temperatures is studied. These understandings are paired with monitoring of the evolution of the SEBS nanostructure at different reaction conditions and/or stages through small-angle X-ray scattering (SAXS), to collectively develop an understanding of how each reaction

mechanism impacts the development of cross-linked precursor nanostructure. Cross-linked SEBS with reaction-altered morphologies can then be converted into OMC upon direct pyrolysis. This work provides key fundamental insights into the implications of solid-state SEBS sulfonation reactions for the interplay between reaction progression and associated structural changes, which can potentially enable the further use of TPEs with process-tunable pore textures and properties.

■ EXPERIMENTAL SECTION

Materials

Polystyrene-block-poly(ethylene-ran-butylene)-block-polystyrene (SEBS) [107 000 g/mol; $\varphi_{\rm PS}=0.21$ (Figures S1 and S2)], toluene (99.5%), and concentrated sulfuric acid (98%) were purchased from Sigma-Aldrich. Deionized (DI) water was obtained by using a Milli-Q IQ 7003 ultrapure purification system (Millipore Sigma). Quartz capillary tubes with an outside diameter of 1 mm for SAXS experiments were purchased from Charles Supper Co. Sodium chloride (NaCl, ACS grade) was purchased from VWR, and sodium hydroxide (NaOH, ACS grade) was purchased from Fisher Chemical.

Synthesis of OMC from Cross-Linked SEBS

In a typical synthesis, 0.5 g of neat SEBS polymer (flaky powder) was introduced into a round-bottom reaction vessel, along with a PTFE (polytetrafluoroethylene)-coated magnetic stir bar. Five milliliters of concentrated sulfuric acid was added to the vessel, and the vessel was placed into a bath of thermal beads that was preheated to a desired reaction temperature (from 100 to 145 °C). After the intended reaction time was reached, the flask was removed and cooled to room temperature. (Note: Safety should be the first priority in any research effort, and using sulfuric acid at increased temperatures can pose various safety risks. Sulfuric acid is corrosive and can release harmful fumes and should be used in only a properly ventilated fume hood while wearing the proper personal protective equipment.) Subsequently, the contents of the vessel were transferred to a glass fritted funnel to remove excess liquids. The polymer was then washed three times with 200 mL of DI water to remove residual acid and other byproducts. After being washed, the polymer was dried under a vacuum at 40 °C overnight. Carbonization of cross-linked SEBS was carried out by placing the cross-linked polymer in an alumina boat, which was then loaded into a tube furnace (OTX-1200, MTI Corp.). The sample was heated under a N₂ atmosphere from room temperature to 600 °C at a ramp rate of 1 °C/min, followed by heat to 800 °C at a rate of 5 °C/min. As a brief note, a seminal work in leveraging polymer precursors for carbon conversion established that a slow ramp to the point at which carbonization (600 °C) occurs assists in maintaining ordered structures.⁶ After this point, the ramp rate can be increased to reduce the carbonization times.

Characterization

The PS volume fraction of the SEBS precursor was determined through nuclear magnetic resonance (NMR) spectroscopy experiments, which were performed using a Bruker 400 MHz spectrometer with a sample concentration of 10 mg/mL in deuterated chloroform. The $^1\mathrm{H}$ spectrum was recorded with 32 proton scans and proton relaxation delays of 5 s. Briefly, the peak associated with the proton bound to the tertiary carbon of the polystyrene repeat unit was set to 1, and the other peaks were integrated with respect to this value. The relative number of moles associated with each peak (n) is determined by dividing the area of the specific peak (A) by the theoretical number of protons associated with that peak (N).

$$n = \frac{A}{N} \tag{1}$$

The relative number of moles for each component was then converted to estimated volume fractions (ϕ_x) using the following equation:

$$\phi_{x} = \frac{\frac{n_{x}m_{w,x}}{\rho_{x}}}{\sum \frac{n_{i}m_{w,i}}{\rho_{i}}} \tag{2}$$

where n_x is the relative number of moles of component x determined through eq 1, $m_{w,x}$ is the molecular weight of the repeat unit of component x, and ρ_x is an estimated density of that component. The denominator is the summation of the relative volumes of the styrene, ethylene, and butylene components of the SEBS precursor.

The mass gain of the sulfonated SEBS polymers was determined by comparing the mass of the polymer before the reaction to the mass of the recovered material after cross-linking, washing, and drying steps as described in the previous section. Specifically, the samples were weighed immediately after removal from a vacuum oven (dried at 100 °C under vacuum for 24 h) to minimize the opportunity of the material to absorb atmospheric humidity. The gel fraction was determined by stirring 0.2 g of polymer in 5 g of toluene for 3 h. The solid was filtered from the toluene and dried, and the final mass was compared to the initial mass prior to soaking in toluene. The degree of sulfonation was determined using Mohr's titrations, which have been described previously.³³ Briefly, 0.2 g of polymer was soaked in a 0.2 M sodium chloride (NaCl) solution for 2 days to exchange Na⁺ ions with H+ ions attached to the sulfonic acid groups on the SEBS polymer backbone. The solution was titrated using a 0.026 M NaOH solution until a neutral pH was reached, and the amount of NaOH required to neutralize the solution was used to calculate the degree of sulfonation of the material using the following equation:

$$\text{degree of sulfonation} = \frac{V_{\text{NaOH}} M_{\text{NaOH}}}{\frac{m_{\text{SEBS}}}{M_{\text{w,SEBS}}} N}$$
(3)

where V_{NaOH} is the volume of NaOH added to the solution once neutralization is achieved, M_{NaOH} is the molarity of the solution, m_{SEBS} is the mass of the SEBS soaked in the NaCl solution, $M_{\mathrm{w,SEBS}}$ is the molecular weight of the polymer, and N is the number of repeat units.

Fourier transform infrared spectroscopy (FTIR) was used to characterize the chemical composition of polymers as a function of the sulfonation reaction time. This was accomplished using a Nicolet 6700 (Thermo Fisher) average over 32 scans with a resolution of 1 cm $^{-1}$. X-ray photoelectron spectroscopy (XPS) characterization was performed by an ESCALAB Xi+ spectrometer (Thermo Fisher), equipped with a MAGCIS Ar+/Arn+ gas cluster ion sputter gun and a monochromatic Al X-ray source (1486.6 eV). A takeoff angle of 90° from the surface was employed, and the base pressure was 3 \times 10 $^{-7}$ mbar. The carbon yield of the materials was determined through thermogravimetric analysis (TGA) (Discovery series 550 TGA, TA Instruments), in which samples were heated in a N2 atmosphere from room temperature to 800 °C at a ramp rate of 10 °C/min.

Nitrogen physisorption measurements at 77 K were performed by using a Tristar II 3020 pore size and surface area analyzer from Micromeritics. Surface areas were calculated through Brunauer-Emmett-Teller (BET) analysis, and pore size distributions were determined through nonlocal density functional theory (NLDFT) for slit pores. Scanning electron microscopy (SEM) was employed to image pore morphologies of carbonized samples using a Zeiss Ultra 60 field-emission SEM instrument with a typical accelerating voltage of 17 kV. Image analysis was performed using ImageJ analysis software to determine pore sizes from the SEM images. In situ SAXS experiments were performed at beamline 12-ID-B of the Advanced Photon Source at Argonne National Laboratory. An X-ray energy of 13.3 keV was used to probe a q range of $\sim 0.034-8.8$ nm⁻¹. Twodimensional scattering patterns were azimuthally averaged to reduce the data to one-dimensional results using MATLAB programs developed by beamline scientists at 12-ID-B. Samples were prepared by introducing a small particle (~1 mg) of polymer into the capillary tube, followed by the introduction of 0.1 mL of H2SO4. A temperature-controlled sample stage was preheated to the desired temperature, and the sample holder containing the capillary tube was introduced into the stage. Scans were manually recorded at varying time intervals throughout the reaction progress. Domain spacings

were calculated through the relationship $d=2\pi/q$, where d is the domain spacing and q is the position of the primary scattering peak in inverse nanometers. Full width at half-maxima (FWHM) were calculated in Igor data analysis software by fitting the primary scattering peak to a single Gaussian. Additionally, cylinder diameters were extracted from one-dimensional scattering patterns by fitting the patterns to generalized scattering functions represented by eq 4:

$$I(q) = F(q) \times S(q) + \text{background}$$
 (4)

where I(q) is the total scattering intensity, F(q) is a flexible cylinder form factor, and S(q) is the structure factor. All model fitting was performed using SASview software, and detailed explanations of the form factor and structure factor employed are present in the literature (more descriptions are also available in the Supporting Information). ^{34,35}

■ RESULTS AND DISCUSSION

The use of SEBS for synthesizing OMCs was recently developed through a two-step process, including a sulfonation-induced cross-linking reaction and subsequent carbonization.¹⁷ Specifically, SEBS was submerged in concentrated sulfuric acid at increased temperatures, allowing the polyolefin matrix to become an efficient carbon precursor. 36-39 During this step, sulfonic acid groups are first attached to both the aromatic ring of the PS repeat unit and the PEB polymer backbone. Subsequently, the sulfonic acid groups in the PEB block can dissociate and then form unsaturated bonds that can undergo cross-linking through multiple reaction intermediates. This approach can lead to an OMC with large mesopore sizes of >10 nm using commercially available SEBS precursors. It is worth mentioning that the use of concentrated sulfuric acid at increased temperatures can raise safety concerns and that safety should be a priority when conducting research that involves these processes. For additional perspective, similar processes are used at industrial scales for the extraction of ores in mining and for the processing of cellulosics in the paper industry. 40 A common method for addressing this issue is through wet flue gas desulfurization using porous alkalinebased sorbents. Compared with previous reports of OMC synthesis through direct pyrolysis of block copolymers (BCPs), which largely involves polyacrylonitrile-based systems, SEBSderived OMCs have several distinct advantages, particularly including the use of low-cost and widely available precursors. While the initial study suggested that varying the reaction temperature can have a major impact on the kinetics of the simultaneous sulfonation and cross-linking reactions, a fundamental understanding of the reaction conditions for developing the nanostructure and chemistry of precursors is still very lacking. Understanding the mechanisms associated with the altered nanostructures of SEBS precursors during sulfonation-induced cross-linking is critical for rational system design with direct control over final pore textures by tuning precursor self-assembly behaviors.⁴¹ Here, this work focuses on deconvoluting the effects of simultaneous reactions on the nanostructure development of a SEBS precursor, allowing a more complete understanding of the intricate self-assembly and nanostructural rearrangement process during sulfonationinduced cross-linking. Consequently, these results can provide insights into the controlled synthesis of OMCs from using TPE precursors and, more broadly, elucidate fundamental BCP selfassembly mechanisms under non-equilibrium conditions.

Three reaction temperatures (100, 125, and 145 °C) were employed for this study to deconvolute chemical and nanostructural contributions from the sulfonation and cross-

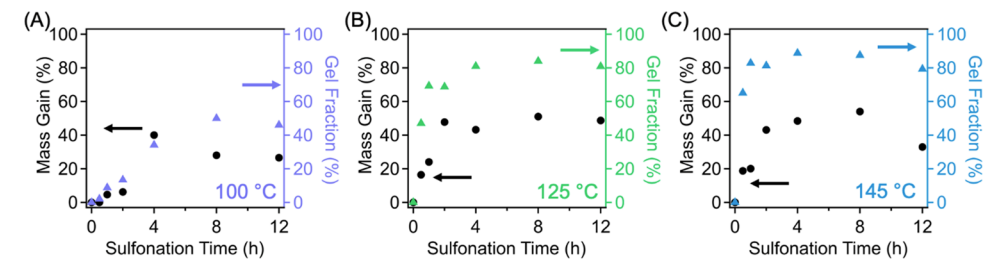


Figure 1. Mass gain and gel fraction results as a function of sulfonation time for SEBS precursors that reacted at (A) 100, (B) 125, and (C) 145 °C.

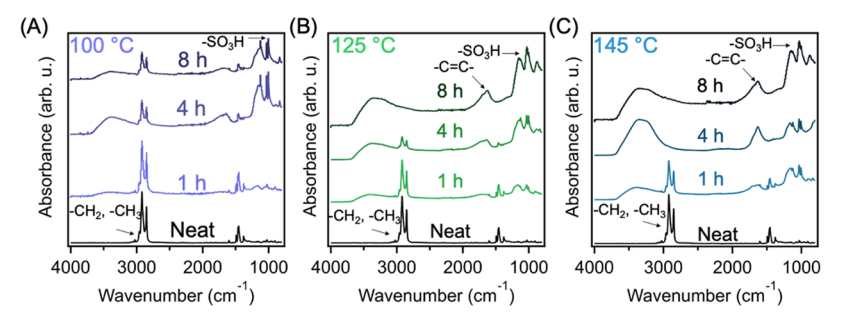


Figure 2. FTIR spectra of SEBS precursors as a function of sulfonation time at (A) 100, (B) 125, and (C) 145 °C.

linking of different segments within SEBS precursors. The progress of the reaction at each temperature was first monitored by determining the mass gain of the samples as a function of sulfonation reaction time as well as their gel fraction (Figure 1). It is important to highlight that because the reaction occurs in the solid state, the progress of the reaction is partially controlled by the ability of the concentrated sulfuric acid to diffuse throughout the SEBS powders. Thus, shorter reaction times may result in largely heterogeneous reactions between the polymer powders and the sulfuric acid. At 100 °C, SEBS exhibits a gradual increase in both the mass gain and gel fraction (Figure 1A) within the first 12 h, reaching values of 27% and 46%, respectively, although a slight decrease is observed after reaction for 4 h. This is potentially due to the loss of sulfonic acid groups to form double bonds, as it has been previously reported to be associated with polyolefin sulfonation at 100 °C.42 The mass gain and gel fraction of samples reacted at 125 and 145 °C are displayed in panels B and C, respectively, of Figure 1. Increased reaction temperatures result in significantly larger gel fractions that increase rapidly within the first 4 h of reaction, reaching 81% and 89% respectively, while faster kinetics are observed in the samples that reacted at 145 °C. Specifically, the mass gain of the sample that reacted at 125 °C approaches a plateau around 4 h of reaction (43%) which is maximized at 8 h (51%). The 145 °C reaction condition approaches a plateau after reaction for 4 h at a value of 48%, which increases slightly to 52% after reaction for 8 h; these mass gain values are similar to those of other studies using polypropylene as a carbon precursor. 43,44 It is worth noting that extension of the reaction at 145 °C to 12 h results in a slightly decreased value for both mass gain and gel fraction. It is observed that this sample breaks down into very fine powders after reaction (Figure S3), suggesting that the decreased mass gain and gel fraction are potentially due to significant degradation/scission of the polymer chains becoming prevalent at long reaction times suggesting oversulfonation. 45,46

The evolution of the chemical composition of SEBS throughout exposure to concentrated sulfuric acid at 100,

125, and 145 °C as a function of time (1, 4, and 8 h) is characterized through Fourier transform infrared spectroscopy (FTIR) in Figure 2. From these spectra, there are multiple characteristic vibrations that can be used to monitor the reaction progress. Specifically, the alkyl stretching vibrations between 2850 and 2920 cm⁻¹ represent reactive sites along the polyolefin backbone that diminish in number as the sulfonation and cross-linking reactions proceed. It is observed that this band is present throughout all reaction times at 100 °C, while its intensity is greatly reduced after 8 and 4 h for the 125 and 145 °C reaction conditions, respectively. The retained presence of the alkyl stretching vibrations indicates that 100 °C is insufficient to completely react and cross-link the polymer backbone, even at extended time scales. Additionally, while it appears that the stretches are completely absent in the FTIR spectra, we note that it is possible that weak bands are present but convoluted within the broad vibration between 3000 and 4000 cm⁻¹. The broad band present in all reacted samples between 1500 and 1930 cm⁻¹ represents a convolution of functional group vibrations, including ketones, aldehydes, and carboxylic acids, which are a result of the sulfonation reactions. Additionally, vibrations associated with the formation of alkenes along the polymer backbone, corresponding to a band at 1629 cm⁻¹, occurred from the dissociation of sulfonic acid groups as one of the intermediates of the sulfonation-cross-linking reaction. The presence of alkenes is greatly pronounced in the samples that reacted at 145 °C, as well as after exposure to the 125 °C reaction condition for 8 h. The two bands at 1000 and 1030 cm⁻¹ correspond to the addition of sulfonic acid groups to the aromatic ring of the PS repeat unit and the polyolefin backbone, respectively; both are present in all samples shown in Figure 2, indicating that the sulfonation reaction can occur even at low temperatures and short time scales. However, samples that reacted at 145 °C exhibit vibrations at 1030 cm⁻¹ that are more intense than those of the other reaction conditions, indicating that sulfonation of the polyolefin majority phase is significantly enhanced at higher temperatures. Additionally, part of the broad stretch between 3000 and 4000

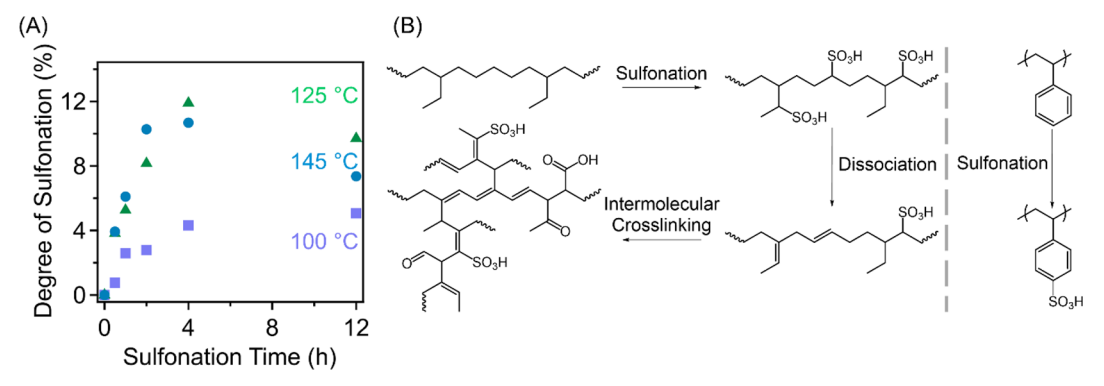


Figure 3. (A) Degree of sulfonation of SEBS as a function of reaction temperature and time determined through Mohr's titrations. (B) Generalized reaction scheme of the sulfonation, dissociation, and cross-linking process that occurs in the PEB majority phase of SEBS precursors at increased temperatures, as well as the sulfonation of the polystyrene phase.

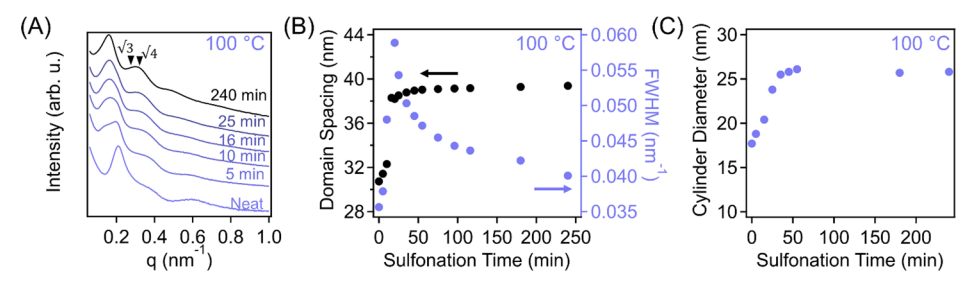


Figure 4. (A) Representative scans from *in situ* SAXS experiments conducted at 100 °C. (B) Corresponding domain spacing and fwhm values determined through the primary ordering peak within the SAXS patterns. (C) Cylinder diameters extracted from model fitting results to represent the growth of the PS minority domains during the sulfonation reaction.

cm⁻¹ could likely be a result of water adsorbed into the material, as the sulfonated polymer becomes very hygroscopic and can ambiently adsorb water from the atmosphere.

These FTIR results are further supported through understanding the degree of sulfonation of SEBS samples determined through Mohr's titrations as functions of the reaction time and temperature, as presented in Figure 3. Reaction at 100 °C results in a steady increase in the amount of sulfonic acid groups in the polymer, achieving a 5% degree of sulfonation after 12 h. The degree of sulfonation of the samples that reacted at 125 °C increases more rapidly to 12% after 4 h. After reaching this maximum, the degree of sulfonation decreases to 10% as a result of the dissociation of sulfonic acid groups during an intermediate step of the cross-linking reaction. This intermediate step is described in the generalized reaction mechanism in Figure 3B. The degree of sulfonation of the samples that reacted at 145 °C also increases rapidly at short reaction times, although the addition of sulfonic acid groups slows from 3 h (10%) to 4 h (11%). This indicates that equilibrium between the addition and dissociation of sulfonic acids during the cross-linking reaction is reached at shorter times at higher reaction temperatures. After reaction for 12 h, the degree of sulfonation is further reduced to 7%. The consistently lower degree of sulfonation in the 145 °C sample than in the 125 °C sample can be attributed to the enhanced kinetics of dissociation of sulfonic acid from PEB backbones at a higher temperature, altering the dynamic equilibrium. These results also indicate that after cross-linking is maximized, longer reaction times can result in further dissociation of the sulfonic acid groups. It is noteworthy that no reduced degree of sulfonation in SEBS samples cross-linked at 100 °C suggests that acid dissociations and cross-linking of the olefinic major block may only minimally occur. It is worth

noting that while the addition of sulfonic acids to the polyolefin backbone and the aromatic group of the polystyrene segments is one major product of exposure to concentrated sulfuric acid at increased temperatures, multiple other functional groups can also be formed as byproducts, such as carboxylic acids, aldehydes, and ketones, as the acid oxidizes the polymer backbone. These are represented in the reaction mechanism and contribute to the mass change of the samples as the reaction time increases. Figure S4 depicts the estimated contribution to mass gain from the addition of sulfonic acid groups through the degree of sulfonation values at each time point. At short times, the experimental and projected mass gains from the degree of sulfonation agree quite well but begin to deviate at longer reaction times for all temperatures, as secondary reactions begin to occur with formation of additional byproducts.

The nanostructural evolution of SEBS reacted at 100 °C was investigated through in situ SAXS experiments (Figure 4A), in which the primary scattering peak was used to extract the domain spacing and fwhm as a function of sulfonation time (Figure 4B). The neat polymer has a primary peak that corresponds to a domain spacing of 30.7 nm and higher-order scattering peaks located at a $1:\sqrt{3}:\sqrt{7}$ ratio, indicating a hexagonally packed cylindrical morphology. After reaction for 5 min, the primary peak becomes distorted, which is caused by the presence of multiple different populations of SEBS domains with distinct sizes that occur due to the diffusion progress of the acid within bulk SEBS samples. Specifically, because the reaction occurs in the solid state and is dependent on the diffusion of acid throughout the polymer particles, the SAXS patterns represent an ensemble of domain spacings present at varying depths within the sample, thus resulting in a convoluted primary scattering peak. After 10 min, the shape of

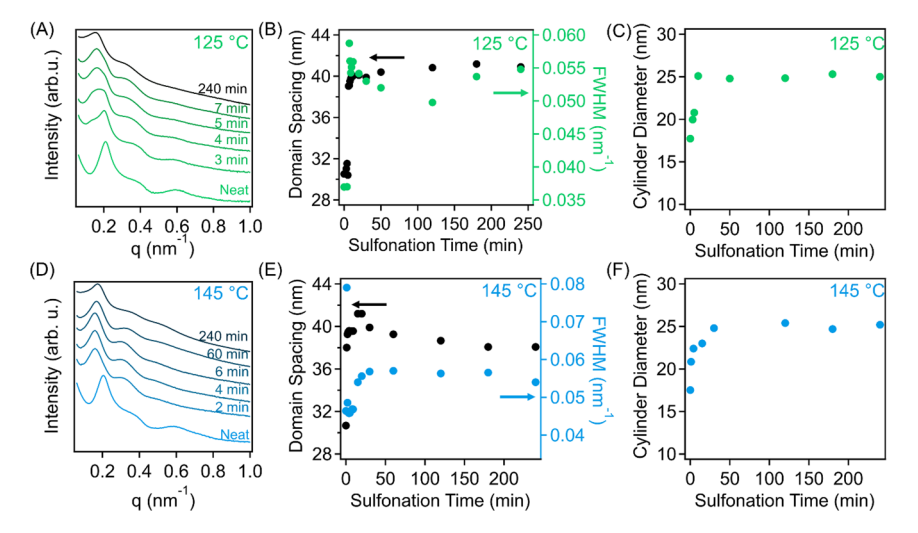


Figure 5. (A) Representative scans from *in situ* SAXS experiments conducted at 125 °C. (B) Corresponding domain spacing and fwhm values determined through the primary ordering peak within the SAXS patterns. (C) Cylinder diameters extracted from model fitting represent the growth of the PS minority domains during the sulfonation reaction. (D) Representative scans from *in situ* SAXS experiments conducted at 145 °C. (E) Corresponding domain spacing and fwhm values determined through the primary ordering peak within the SAXS patterns. (F) Cylinder diameters extracted from model fitting represent the growth of the PS minority domains during the sulfonation reaction.

the primary peak became symmetric and was retained throughout the 4 h measurement window (4 h is the maximum reaction time investigated through SAXS). Although the reaction continues to progress after 4 h, SAXS patterns demonstrate minimal changes in the sample nanostructure on lengthened time scales. As shown in Figure 4B, the domain spacing increases to 38.3 nm during the first 20 min of reaction, after which the rate of swelling slows and plateaus at a domain spacing of 39.2 nm. Furthermore, the FWHM can be used to evaluate the degree of ordering in the SEBS nanostructure and demonstrates an initial significant increase in the degree of disorder degree associated with the nanostructural rearrangement at an early stage. However, after the plateau in domain spacing is reached and swelling of the BCP domains ceases, the FWHM continuously decreases as the degree of nanostructural ordering is further developed in the sulfonated SEBS. After reaction for 4 h, the FWHM decreases to 0.040 nm⁻¹ and the scattering pattern exhibits a strong higher-order scattering peak.

Interestingly, despite the addition of sulfonic acid groups to both polymer constituents, high-order peaks from SAXS patterns became more pronounced throughout the progression of the reaction. This suggests the presence of polymer mobility for encouraging structural rearrangement and ordering development in a low-temperature sulfonation system (at 100 °C), while the improved packing/ordering of SEBS nanodomains is potentially a result of ionic repulsion between the polymer constituents effectively increasing their χ . Specifically, the acidic environment during the sulfonationinduced cross-linking reaction can deprotonate the sulfonic acid groups along the polymer backbone, resulting in negatively charged species within the majority and minority phases. Consequently, these charges effectively increase the incompatibility between the blocks and promote an increased level of order. Analogous results are observed in the formation of charged block copolymer micelles where the micelle morphology is dependent on the amount of electrostatic repulsion between charged repeat units in the micelle corona. 47,48 Specifically, more pronounced electrostatic repulsion between charged units results in extended micelle

coronae and smaller aggregation numbers, which could be used to explain the electrostatic repulsion between sulfonate groups in both blocks of the SEBS precursor to establish improved degrees of order. Additionally, it has been found that the introduction of charged groups into block copolymers may result in a significantly altered phase diagram. Olvera de la Cruz et al. have demonstrated that asymmetrically charged polymers exhibit a greatly shifted phase diagram due to electrostatic cohesion within the selectively charged block.45 However, as mentioned previously, both blocks of the reacted SEBS precursor contain sulfonic acid groups. Increases in domain spacing can be determined to be a function of an increased Flory-Huggins interaction parameter (χ) between the blocks as well as an increased volume fraction of the minority phase. In the strong segregation limit, the domain spacing scales at $\chi^{0.1667}$ and approximately $\varphi^{0.1875}$ for cylindrical systems. It is hypothesized that an increase in χ is associated with a concomitant increase in φ ; thus, volume fraction increases are the dominant mechanism for driving the nanostructural rearrangement. 50 The cylinder diameter of the PS minority phase was extracted through fitting the scattering patterns to a generalized scattering function that contained a flexible cylinder form factor to represent the size and shape of the PS cylinders. For fitting, the scattering contrast of the PS and PEB phases was considered to be constant throughout the course of the reaction, the domain spacing extracted from the primary peaks in the scattering patterns was employed as a constant, and a cylinder radius dispersity ratio of 0.2 was employed across all fits. Representative fits can be found in Figure S5, and their corresponding fitting parameters are listed in Table S1. Figure 4C shows that the neat SEBS polymer has a cylinder diameter of 17.7 nm, which steadily increases to 26.1 nm throughout the first 1 h of reaction and remains virtually constant throughout the experimental window. Comparing this result to the increased domain spacing after reaction for 1 h (39.0 nm), we found that the expansion of the PS minority phase through the addition of sulfonic acid groups is primarily responsible for the domain expansion.

In situ SAXS results for the 125 and 145 °C reaction conditions are shown in Figure 5. The SAXS patterns

Figure 6. (A) Representative mechanism for the carbonization of the cross-linked SEBS material based on a previous similar work. (B) Carbon yields for the SEBS samples sulfonated at 125 and 145 °C determined through TGA.

associated with the 125 °C reaction (Figure 5A) exhibit a nanostructural rearrangement at short reaction times, where the domain spacing in the neat polymer (30.5 nm) increases to the initial plateau (40.1 nm) within just 12 min of reaction. The initial nanostructural rearrangement is accompanied by a sharp increase in the value of FWHM (Figure 5B), also observed under the 100 °C reaction conditions, which later decreases as order is improved in the system throughout the reaction. However, the FWHM begins to increase after reaction for 2 h, which can be attributed to the initiation of cross-linking after the attachment and detachment of sulfonic acid groups from PEB backbones (Figure 3B). It has been established that cross-linking of BCPs can significantly impact the ability to assemble into ordered nanostructures. 51-53 For instance, Hickner et al. developed polystyrene-based BCPs that were selectively cross-linked through olefin metathesis for application as anion exchange membranes.⁵⁴ While the neat BCPs exhibited high degrees of order, their cross-linked counterparts became less ordered, and the reassembly into ordered nanostructures became challenging. Corresponding PS cylinder diameter results from fitting the SAXS patterns to the previously mentioned scattering functions are provided in Figure 5C. The minority PS phase swells from an initial value of 17.7 nm in the neat sample to 25.1 nm after sulfonation for 10 min. This value is maintained throughout the 4 h reaction. Notably, the cylinder diameter is decreased in comparison to that under the 100 °C reaction condition. Additionally, comparing the cylinder diameter to the domain spacing of the polymer (40.1 nm) suggests that the PS minority phase represents 63% of the overall domain spacing; we note previous simulation results indicated that such an inverse cylindrical morphology exists in self-assembled, chargecontaining BCP systems. 49 The majority phase also exhibits a slight expansion from 12.8 to 15.0 nm. These results indicate that cross-linking limits the degree of domain expansion of SEBS samples. The sample that reacted at 145 °C exhibits a similar mechanism for the rearrangement of the nanostructure during the course of the reaction. However, it is noted that the effects of the reaction on the nanostructure occur much more rapidly. The SAXS patterns in Figure 5D indicate that the nanostructure is rearranged within 2 min of reaction associated with an increase in domain spacing from 30.7 to 39.5 nm. The domain expansion is further investigated through calculated cylinder diameters as a function of reaction time (Figure 5F). The cylindrical minority phase (17.5 nm) swells as a result of reaction, but the cylinder diameter achieves an equilibrium value of 24.8 nm after 30 min. Therefore, it is found that the expansion of the cylindrical minority phase is more limited at 145 °C than at lower reaction temperatures, and the increase in domain spacing is established at time scales shorter than that

in the sample that reacted at 125 °C. These results, along with results from Figures 1 and 2, suggest that the reaction within the PEB matrix plays a more significant role at higher temperatures. The enhanced reaction rate of the PEB phase at increased temperatures results in more confined expansion of the PS domains due to competition with the cross-linking reaction of the PEB matrix. However, the PS expansion is still dominant and represents 63% of the domain spacing for samples cross-linked at 145 °C. The SAXS results indicate that longer reaction times exhibit slight decreases in domain spacing (note the cylinder diameter remains constant), which may be attributed to the cross-linking-induced densification of the majority phase. As shown in Figure 5F, at 145 °C the fwhm of SEBS samples begins to increase after reaction for 6 min and reaches a plateau at ~60 min. As observed under the 125 °C reaction condition, this increased level of disorder can be associated with the onset of the cross-linking reaction, which is accelerated by the increased reaction temperature.

Contributions of sulfonation reactions to the nanostructural changes of SEBS can be deconvoluted as such. The initial addition of sulfonic acid groups to the polymer backbone and aromatic rings of the PS repeating unit results in significantly swelled domain spacings, particularly associated with the size of minority domains. When very limited degrees of crosslinking are observed, sulfonation of both SEBS phases further drives the immiscibility between the blocks, potentially caused by electrostatic repulsion of the ionic sulfonic acid groups. Furthermore, the degree of ordering in the sulfonated SEBS (without cross-linking) is developed during exposure to increased temperatures, which can act as an annealing step. However, under conditions where cross-linking can occur, the onset of cross-linking is accompanied by a decreased level of order in the SEBS nanostructure while the domain spacings remain relatively constant. In these cases, a higher temperature may lead to a reduced cylinder diameter of the PS segment due to the early occurrence of kinetic trapping that limits the domain swelling.

Upon carbonization, the cross-linked network developed during the sulfonation reaction stabilizes the polymer matrix and prevents thermal degradation. In turn, the polymer matrix cyclizes and functional groups are decomposed, leaving an amorphous carbon framework behind (Figure 6A). This mechanism has been described previously. The carbon yield of the samples that reacted at 125 and 145 °C was investigated through TGA to maximize yield with minimum reaction time under both reaction conditions (Figure 6B). We note that while the 100 °C reaction temperature exhibits a significant gel fraction after 12 h, this does not necessarily correlate to the degree of intermolecular cross-linking (a necessary step for enabling their use as carbon precursors) in

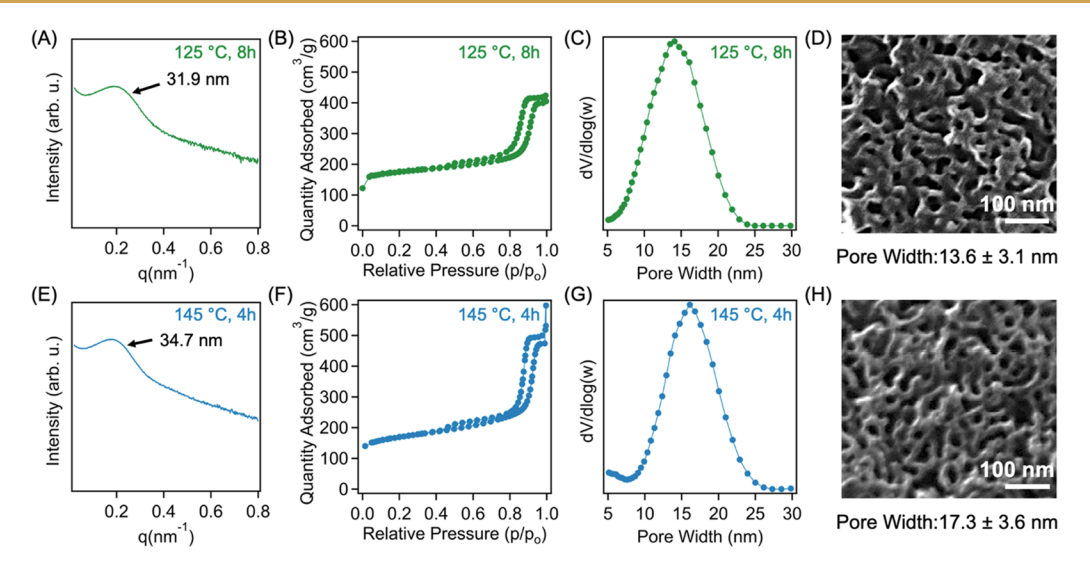


Figure 7. (A) SAXS pattern, (B) liquid nitrogen physisorption isotherm, (C) NLDFT pore size distribution, and (D) SEM image of SEBS-derived OMCs that reacted at 125 °C for 8 h. (E) SAXS pattern, (F) liquid nitrogen physisorption isotherm, (G) NLDFT pore size distribution, and (H) SEM image of SEBS-derived OMCs that reacted at 145 °C for 4 h.

all systems. This is supported by Figure S6, which demonstrates that even after reaction for 12 h, no considerable carbon yield (<4 wt %) is observed. Representative TGA thermograms for samples reacted for 1, 4, 8, and 12 h at 125 and 145 °C are provided in Figure S7. Both reaction conditions result in steadily increasing carbon yields with longer reaction times as cross-linking progresses throughout the material. This cross-linking progress can also be tracked through SEM, and representative images of the polymers that reacted at 125 °C after carbonization are presented in Figure S8. Specifically, at early reaction times, the interior of the particle completely decomposes, leaving only a carbonized shell behind. This is a result of the acid not fully diffusing into the center of the particle, leaving it un-cross-linked and susceptible to thermal degradation. As the reaction time increases, the carbonized shell thickens until a continuous carbon particle is formed. This is consistent with previous works that employed the diffusion control of the cross-linking sulfuric acid to form hollow fibrous structures in other polyolefin materials. ^{39,44} The carbon yield increases much more rapidly at 145 °C than at 125 °C, in good agreement with results from Figures 1 and 2 due to their improved crosslinking reaction kinetics. For example, after reaction for 1 h, the sample that reacted at 125 °C produces a carbon yield of 9 wt %, while the sample that reacted at 145 $^{\circ}\text{C}$ exhibits a carbon yield of 25 wt %. These values increase to 27 and 39 wt % for reaction temperatures of 125 and 145 °C, respectively, at a time of 4 h, after which they continue to increase to 40% and 46%, respectively, when the reaction time is extended to 12 h.

The impact of reaction temperature, including 125 °C (for 8 h) and 145 °C (for 4 h) as representative examples, on the structures of carbonized mesoporous materials is characterized through SAXS, nitrogen physisorption, and SEM in Figure 7. The samples were heated to 600 °C at a ramp rate of 1 °C/min, followed by a ramp to 800 °C at a ramp rate of 5 °C/min. As mentioned previously, the slower ramp at lower temperatures could assist in maintaining ordered structures as the system approaches the temperature at which carbonization occurs. As a note, nitrogen physisorption isotherms for additional reaction times at 125 and 145 °C are found in

Figures S9 and S12, while their associated pore size distributions are demonstrated in Figures S10 and S13; SEM micrographs of the carbonized pore structures are presented in Figures S11 and S14. After sulfonation-enabled cross-linking and subsequent carbonization, SEBS-derived OMCs crosslinked at 125 °C with short reaction times exhibit highly disordered pore size distributions, which were calculated through nonlocal density functional theory (NLDFT) from the physisorption isotherms (Figure S10) until the reaction had proceeded for 4 h. Briefly, the use of NLDFT is an established and versatile method for determining pore sizes in porous materials through nitrogen physisorption experiments, 56-58 accomplished by determining the equilibrium adsorption state of the nitrogen probe through calculating the density of the fluid within the pore. The disorder in the carbon products from samples that were first cross-linked for shorter time periods is caused by insufficient cross-linking, rendering the system incapable of retaining the ordered structures for pyrolysis and their conversion to carbons, although some carbon is produced. This is also supported through the SEM micrographs that indicate the absence of the ordered mesopores in both the 1 and 2 h samples, but they are present after reaction for at least 4 h. The sample that reacted for 8 h at 125 °C exhibits a relatively broad primary scattering peak (Figure 7A), indicating a domain spacing of 31.9 nm and a FWHM of 0.12 nm⁻¹. These results show that the OMC nanostructures are significantly disrupted in comparison to that of the cross-linked SEBS precursor as a result of the hightemperature carbonization process. Furthermore, the nitrogen physisorption isotherm (Figure 7B) exhibits a typical type IV isotherm that is characteristic of mesoporous materials, 56-58 and the pore size distribution indicates an averaged pore population of 14.8 nm with a FWHM of 8.3 nm. Additionally, ordered pore structures are also observed in the scanning electron micrograph in Figure 7D. From image analysis using ImageJ, the pores within the image have an average pore width of 13.6 nm, which is in agreement with the results obtained through physisorption experiments. The samples that reacted under the 145 °C reaction condition establish order at much shorter reaction times, as indicated by the appearance of the

type IV isotherm after cross-linking and carbonization for 1 h, as well as uniform pore size distributions. This is supported by the faster cross-linking kinetics determined throughout this work. SEM micrographs also depict the presence of ordered mesopores at time scales of ~ 1 h, although it is worth noting that order begins to be disrupted after reaction for 12 h, where the pore size distribution becomes much broader and a large amount of micropores is introduced into the sample. A SAXS pattern of the sample reacted at 145 °C for 4 h and subsequently carbonized is depicted in Figure 7E. The primary scattering peak indicates a slightly larger domain spacing of 34.7 nm and a FWHM of 0.12 nm⁻¹. The nitrogen physisorption isotherm in Figure 7F also demonstrates mesoporous character, and the NLDFT pore size distribution exhibits an average pore size of 16.1 nm. Furthermore, SEM imaging confirms the cylindrical pore morphology with average pore widths of 17.3 nm. We note that the retention of ordered nanostructures upon conversion of cross-linked SEBS to OMC also suggests that a cylinder-forming morphology was retained even after polystyrene experienced significant swelling upon sulfonation; in the case of an order-to-order morphology transition (from cylinder to lamellae), ordered layered structures would be collapsed upon removal of polystyrene domains. Together, the varied processing conditions for SEBS cross-linking result in similar pore morphologies, with variations in pore size and domain spacing. In particular, while cross-linked SEBS samples at distinct sulfonation temepatures have similar domain spacing, 145 °C samples exhibit less domain shrinkage (~13%) compared to their counterparts that were cross-linked at 125 °C (~20%). This can be attributed to improved framework integrity cross-linked at higher temperatures, suggesting the opportunity to obtain different OMC pore sizes through simply varying processing conditions while using the same SEBS precursor.

Figure 8 further investigates the systemic differences in pore textures of SEBS-derived OMCs prepared by different cross-

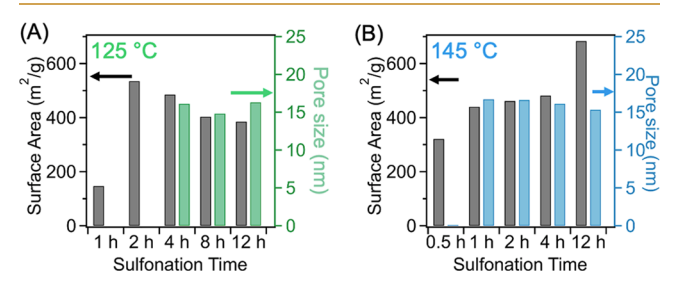


Figure 8. Surface areas and pore sizes of SEBS-derived OMCs, which are cross-linked for different amounts of time at 145 °C.

linking conditions. Specifically, nitrogen physisorption experiments at 77 K were employed to determine the effect of cross-linking time on the pore textures of the carbonized materials. For samples cross-linked at 125 °C, carbon is produced after cross-linking and subsequent carbonization for 1 h; however, the surface area is very small, and there are no ordered pores. Increasing the reaction time to 2 h enhances the surface area to 535 m²/g, but cross-linking is still insufficient to stabilize the ordered porous structure. After reaction for 4 h, order is established, and the physisorption isotherm indicates an averaged mesopore size of 16.1 nm and a surface area of 485 m²/g. Extending the reaction time to 12 h leads to a reduced BET surface area of 385 m²/g and a very similar pore size distribution profile, indicating a limited change in the overall

pore texture. Furthermore, as shown in Figure 8, shorter reaction times (<1 h) at 145 °C result in disordered microporous structures, indicating structural collapse from insufficient cross-linking. For instance, after reaction for 0.5 h, the corresponding OMC exhibits a BET surface area of 321 m²/g, but only a disordered distribution of pores is present. Reaction for 1 h at 145 °C is sufficient to produce ordered pores with an averaged pore size of 16.7 nm and a BET surface area of 440 m²/g. The pore size and surface area are generally maintained through the 4 h reaction (\sim 16.1 nm and \sim 481 m²/ g, respectively). However, the fwhm values of the pore size distribution decrease from 9.5 nm for cross-linking for 1 h to 7.9 nm for cross-linking for 4 h, indicating an improved degree of ordering is attained. After reaction of the SEBS precursor for 12 h at 145 °C, the surface area of the resulting OMC greatly increases to 683 m²/g while a very broad pore size distribution is observed with the peak centered at 15.3 nm. This suggests the formation of a large amount of micropores, evidenced in Figure S13E, which greatly enhances the surface area of the product. This result further indicates that extending the reaction time may result in disruption of the ordered nanostructure, leading to degradation processes and the formation of micropores. For comparison, the surface areas of these SEBS-derived OMCs are slightly smaller than those of conventional soft-templated OMCs using structure-directing agents, which can approach and exceed 700 m²/g.⁵ However, reduced surface areas are common in large-pore OMCs and are consistent with multiple literature examples. 62-64 It is worth mentioning that the sulfonation-induced cross-linking reaction inherently dopes sulfur heteroatoms into the carbon framework after carbonization. The sulfur content in the carbonized samples was investigated through X-ray photoelectron spectroscopy (XPS) survey scans, and the results are present in Figure S15 and Table S2. Generally, increased reaction times result in larger amounts of sulfur of 0.5 and 0.9 atom % in the samples that were cross-linked for 2 and 8 h at 125 °C, respectively. Similar results are observed for the 145 °C reaction condition, although the sulfur contents are slightly higher at the same reaction times. The increased sulfur content in final OMC products, with an increase in crosslinking time, suggests that a more cross-linked precursor network may have a stronger ability to retain heteroatom functional groups in the carbon framework upon pyrolysis. Overall, this work demonstrates the impact of sulfonation and cross-linking on SEBS morphology development, pore textures, and carbon characteristics of the resulting sulfur-doped OMC products.

CONCLUSIONS

ı

Sulfonation-induced cross-linking of nanostructured thermoplastic elastomers (TPEs) has been established as an effective route for the synthesis of OMCs. However, as this reaction occurs within the solid state, resulting in simultaneous reactions in all segments in SEBS precursors, the impacts of the reaction on precursor nanostructure development are complicated. Understanding the influence of the heterogeneous cross-linking reaction on the self-assembly behaviors of the SEBS precursor is important to enable its ability to potentially tailor the resulting OMC material properties through manipulating reaction conditions. In this work, upon variation of the reaction temperature (100, 125, and 145 °C), deconvolution of these reactions within the distinct domains of a SEBS precursor can be accomplished, allowing the

investigation of their respective contributions to precursor morphology evolution. It is found that cross-linking of a polyolefinic matrix occurs only at temperatures of >100 °C. Sulfonation of the polstyrene phase in the absence of crosslinking results in considerable swelling of the cylindrical domains from 17.7 to 26.1 nm. At higher temperatures, sulfonation of polyolefin domains becomes prevalent and cross-linking occurs, resulting in limited domain swelling of the altered nanostructure. The effects of the temperature-dependent nanostructural changes within the precursors on the pore characteristics of carbonized and noncarbonized OMCs were also investigated. Generally, although cross-linking reduces the level of order in the self-assembled BCP nanomaterials, obtaining a sufficient degree of cross-linking in SEBS-based precursors is necessary to stabilize the structure during carbonization, allowing the formation of ordered mesopores. While carbon is formed at short reaction times, order in the pore structures from using SEBS precursors is established only after sufficient cross-linking has occurred, and the level of order increases with further cross-linking until the structure begins to degrade. Further optimization of the processing conditions (e.g., cross-linking time, temperature, and pyrolysis condition) might be useful to further improve the order of the porous structures. Additionally, it is found that higher degrees of crosslinking, which occurs at higher reaction temperatures, can result in OMCs with more limited pore/structural shrinkage during pyrolysis and high sulfur heteroatom content. Collectively, this work demonstrates an important fundamental understanding of how to optimize reaction/processing pathways to control pore textures of SEBS-derived OMCs. These results can inform rational system design for fully enabling the use of TPEs as efficient precursors for OMC synthesis, which may also be further applied to complex BCP systems that undergo reaction-induced nanostructural changes through solid-state reactions.

ASSOCIATED CONTENT

Supporting Information

The Supporting Information is available free of charge at https://pubs.acs.org/doi/10.1021/acsaenm.3c00359.

Characterization of the neat precursor, predicted mass gains from sulfonation, expressions for model functions used to fit scattering data and the associated fit parameters, TGA thermograms, liquid nitrogen sorption isotherms, pore size distributions, SEM micrographs, and XPS results for SEBS-derived OMCs cross-linked at different temperatures (PDF)

AUTHOR INFORMATION

Corresponding Author

Zhe Qiang — School of Polymer Science and Engineering, University of Southern Mississippi, Hattiesburg, Mississippi 39406, United States; orcid.org/0000-0002-3539-9053; Email: zhe.qiang@usm.edu

Authors

Mark Robertson — School of Polymer Science and Engineering, University of Southern Mississippi, Hattiesburg, Mississippi 39406, United States

Andrew Barbour – School of Polymer Science and Engineering, University of Southern Mississippi, Hattiesburg, Mississippi 39406, United States Anthony Griffin — School of Polymer Science and Engineering, University of Southern Mississippi, Hattiesburg, Mississippi 39406, United States; orcid.org/0000-0003-0526-194X

Alejandro Guillen Obando — School of Polymer Science and Engineering, University of Southern Mississippi, Hattiesburg, Mississippi 39406, United States

Paul Smith — School of Polymer Science and Engineering, University of Southern Mississippi, Hattiesburg, Mississippi 39406, United States

Complete contact information is available at: https://pubs.acs.org/10.1021/acsaenm.3c00359

Author Contributions

M.R. and Z.Q. designed the experiments. Sample preparation was carried out by A.B. and M.R., and characterization of the samples was performed by M.R., A.B., A.G.O., A.G., and P.S. All authors contributed to the writing of the manuscript, although it was primarily written by M.R. and Z.Q. Z.Q. also supervised all contributions to this project.

Notes

The authors declare no competing financial interest.

ACKNOWLEDGMENTS

This work was supported by the National Science Foundation (CMMI-2239408). The authors acknowledge the support from the University of Southern Mississippi and Mississippi SMART Business Act. Additionally, M.R. acknowledges the financial support through the DOE SCGSR program. This research used resources of the Advanced Photon Source, a U.S. Department of Energy (DOE) Office of Science user facility operated for the DOE Office of Science by Argonne National Laboratory under Contract DE-AC02-06CH11357. The authors also acknowledge the beamline scientists and support staff at beamline 12-ID-B at the Advanced Photon Source in Argonne National Laboratory for their assistance during X-ray scattering experiments.

REFERENCES

- (1) Ma, T. Y.; Liu, L.; Yuan, Z. Y. Direct Synthesis of Ordered Mesoporous Carbons. *Chem. Soc. Rev.* **2013**, 42, 3977–4003.
- (2) Ndamanisha, J. C.; Guo, L. P. Ordered Mesoporous Carbon for Electrochemical Sensing: A Review. *Anal. Chim. Acta* **2012**, 747, 19–28.
- (3) Eftekhari, A.; Fan, Z. Ordered Mesoporous Carbon and Its Applications for Electrochemical Energy Storage and Conversion. *Mater. Chem. Front* **2017**, *1*, 1001.
- (4) Gao, Y.; Wang, Q.; Ji, G.; Li, A.; Niu, J. Doping Strategy, Properties and Application of Heteroatom-Doped Ordered Mesoporous Carbon. *RSC Adv.* **2021**, *11*, 5361–5383.
- (5) Robertson, M.; Zagho, M. M.; Nazarenko, S.; Qiang, Z. Mesoporous Carons from Self-Assembled Polymers. *J. Polym. Sci.* **2022**, *60*, 2015–2042.
- (6) Meng, Y.; Gu, D.; Zhang, F.; Shi, Y.; Cheng, L.; Feng, D.; Wu, Z.; Chen, Z.; Wan, Y.; Stein, A.; Zhao, D. A Family of Highly Ordered Mesoporous Polymer Resin and Carbon Structures from Organic-Organic Self-Assembly. *Chem. Mater.* **2006**, *18*, 4447–4464.
- (7) Wu, Z.; Webley, P. A.; Zhao, D. Post-Enrichment of Nitrogen in Soft-Templated Ordered Mesoporous Carbon Materials for Highly Efficient Phenol Removal and CO2 Capture. *J. Mater. Chem.* **2012**, 22, 11379–11389.
- (8) Qiang, Z.; Gurkan, B.; Ma, J.; Liu, X.; Guo, Y.; Cakmak, M.; Cavicchi, K. A.; Vogt, B. D. Roll-to Roll Fabrication of High Surface Area Mesoporous Carbon with Process-Tunable Pore Texture for

- Optimization of Adsorption Capacity of Bulky Organic Dyes. *Microporous Mesoporous Mater.* **2016**, 227, 57–64.
- (9) Liu, T.; Liu, G. Block Copolymer-Based Porous Carbons for Supercapacitors. *I. Mater. Chem. A* **2019**, *7*, 23476–23488.
- (10) Kopeć, M.; Lamson, M.; Yuan, R.; Tang, C.; Kruk, M.; Zhong, M.; Matyjaszewski, K.; Kowalewski, T. Polyacrylonitrile-Derived Nanostructured Carbon Materials. *Prog. Polym. Sci.* **2019**, *92*, 89–134.
- (11) Song, Y.; Wei, G.; Kopeć, M.; Rao, L.; Zhang, Z.; Gottlieb, E.; Wang, Z.; Yuan, R.; Ye, G.; Wang, J.; Kowalewski, T.; Matyjaszewski, K. Copolymer-Templated Synthesis of Nitrogen-Doped Mesoporous Carbons for Enhanced Adsorption of Hexavalent Chromium and Uranium. ACS Appl. Nano Mater. 2018, 1, 2536—2543.
- (12) Yuan, R.; Kopeć, M.; Xie, G.; Gottlieb, E.; Mohin, J. W.; Wang, Z.; Lamson, M.; Kowalewski, T.; Matyjaszewski, K. Mesoporous Nitrogen-Doped Carbons from PAN-Based Molecular Bottlebrushes. *Polymer* **2017**, *126*, 352–359.
- (13) Kowalewski, T.; Tsarevsky, N. V.; Matyjaszewski, K. Nanostructured Carbon Arrays from Block Copolymers of Polyacrylonitrile. *J. Am. Chem. Soc.* **2002**, *124*, 10632–10633.
- (14) Wu, D.; Li, Z.; Zhong, M.; Kowalewski, T.; Matyjaszewski, K. Templated Synthesis of Nitrogen-Enriched Nanoporous Carbon Materials from Porogenic Organic Precursors Prepared by ATRP. *Angew. Chem. Int. Ed* **2014**, *53*, 3957–3960.
- (15) Tang, C.; Tracz, A.; Kruk, M.; Zhang, R.; Smilgies, D. M.; Matyjaszewski, K.; Kowalewski, T. Long-Range Ordered Thin Films of Block Copolymers Prepared by Zone-Casting and Their Thermal Conversion into Ordered Nanostructured Carbon. *J. Am. Chem. Soc.* **2005**, *127*, 6918–6919.
- (16) Liu, X.; Chen, W.; Hong, Y. L.; Yuan, S.; Kuroki, S.; Miyoshi, T. Stabilization of Atactic-Polyacrylonitrile under Nitrogen and Air As Studied by Solid-State NMR. *Macromolecules* **2015**, *48*, 5300–5309.
- (17) Robertson, M.; Guillen-Obando, A.; Barbour, A.; Smith, P.; Griffin, A.; Qiang, Z. Direct Synthesis of Ordered Mesoporous Materials from Thermoplastic elastomer. *Nat. Commun.* **2023**, *14*, 639.
- (18) Kim, B.; Kim, J.; Jung, B. Morphology and Transport Properties of Protons and Methanol through Partially Sulfonated Block Copolymers. J. Membr. Sci. 2005, 250, 175–182.
- (19) Kim, J.; Kim, B.; Jung, B.; Kang, Y. S.; Ha, H. Y.; Oh, I. H.; Ihn, K. J. Effect of Casting Solvent on Morphology and Physical Properties of Partially Sulfonated Polystyrene-Block-Poly(Ethylene-Ran-Butylene)-Block-Polystyrene Copolymers. *Macromol. Rapid Commun.* **2002**, 23, 753–756.
- (20) Date, B.; Han, J.; Park, S.; Park, E. J.; Shin, D.; Ryu, C. Y.; Bae, C. Synthesis and Morphology Study of SEBS Triblock Copolymers Functionalized with Sulfonate and Phosphonate Groups for Proton Exchange Membrane Fuel Cells. *Macromolecules* **2018**, *51*, 1020–1030.
- (21) Lu, X.; Steckle, W. P.; Weiss, R. A. Ionic Aggregation in a Block Copolymer Ionomer. *Macromolecules* **1993**, *26*, 5876–5884.
- (22) Lu, X.; Steckle, W. P.; Hsiao, B.; Weiss, R. A. Thermally Induced Microstructure Transitions in a Block Copolymer Ionomer. *Macromolecules* **1995**, *28*, 2831–2839.
- (23) Mani, S.; Weiss, R. A.; Williams, C. E.; Hahn, S. F. Microstructure of Ionomers Based on Sulfonated Block Copolymers of Polystyrene and Poly(Ethylene-Alt-Propylene). *Macromolecules* 1999, 32, 3663–3670.
- (24) Weiss, R. A.; Sen, A.; Pottick, L. A.; Willis, C. L. Block Copolymer Ionomers 2. Viscoeleastic and Mechanical Properties of Sulphonated Poly(Styrene-Ethylene/Butylene-Styrene). *Polymer* 1991, 32, 2785–2792.
- (25) Lu, X.; Steckle, W. P.; Weiss, R. A. Morphological Studies of a Triblock Copolymer Ionomer by Small Angle X-Ray Scattering. *Macromolecules* **1993**, *26*, 6525–6530.
- (26) Eisenberg, A.; Hird, B.; Moore, R. B. A New Multiplet-Cluster Model for the Morphology of Random Ionomers. *Macromolecules* **1990**, 23, 4098–4107.
- (27) Mauritz, K. A.; Blackwell, R. I.; Beyer, F. L. Viscoelastic Properties and Morphology of Sulfonated Poly(Styrene-b-Ethylene/

- Butylene-b-Styrene) Block Copolymers (SBCP), and SBCP/[Silicate] Nanostructured Materials. *Polymer*, **2004**, *45*, 3001–3016.
- (28) Blackwell, R. I.; Mauritz, K. A. Dynamic Mechanical Properties of Annealed Sulfonated Poly(Styrene-b-[Ethylene/Butylene]-b-Styrene) Block Copolymers. *Polymer* **2004**, *45*, 3457–3463.
- (29) Zofchak, E. S.; Lanasa, J. A.; Mei, W.; Hickey, R. J. Polymerization-Induced Nanostructural Transitions Drive by in situ Polymer Grafting. ACS Macro Lett. 2018, 7, 822–827.
- (30) Zofchak, E. S.; Lanasa, J. A.; Torres, V. M.; Hickey, R. J. Deciphering the Complex Phase Behavior during Polymerization-Induced Nanostructural Transitions of a Block Polymer/Monomer Blend. *Macromolecules* **2020**, *53*, 835–843.
- (31) Williams, E. R.; McMahon, P. L.; Reynolds, J. E.; Snider, J. L.; Stavila, V.; Allendorf, M. D.; Stefik, M. Tailored Porous Carbons Enabled by Persistent Micelles with Glassy Cores. *Mater. Adv.* **2021**, 2, 5381–5395.
- (32) Sarkar, A.; Stefik, M. How to Make Persistent Micelle Templates in 24 h and Know it Using X-Ray Scattering. *J. Mater. Chem. A* **2017**, *5*, 11840–11853.
- (33) Wang, Q.; Lu, Y.; Li, N. Preparation, Characterization and Performance of Sulfonated Poly(Styrene-Ethylene/Butylene-Styrene) Block Copolymer Membranes for Water Desalination by Pervaporation. *Desalination* **2016**, *390*, 33–46.
- (34) Pedersen, J. S.; Schurtenberger, P. Scattering Functions of Semiflexible Polymers with and without Excluded Volume Effects. *Macromolecules* **1996**, *29*, 7602–7612.
- (35) Kotlarchyk, M.; Chen, S. H. Analysis of Small Angle Neutron Scattering Spectra from Polydisperse Interacting Colloids. *J. Chem. Phys.* **1983**, *79*, 2461.
- (36) Robertson, M.; Guillen Obando, A.; Nunez, B.; Chen, H.; Qiang, Z. Upcycling Mask Waste to Carbon Capture Sorbents: A Combined Experimental and Computational Study. *ACS Appl. Eng. Mater.* **2023**, *1*, 165–174.
- (37) Younker, J. M.; Saito, T.; Hunt, M. A.; Naskar, A. K.; Beste, A. Pyrolysis Pathways of Sulfonated Polyethylene, an Alternative Carbon Fiber Precursor. *J. Am. Chem. Soc.* **2013**, *135*, 6130–6141.
- (38) Robertson, M.; Griffin, A.; Guillen Obando, A.; Barbour, A.; Davis, R.; Qiang, Z. Precursor Design for Efficient Synthesis of Largepore, Sulfur-doped Ordered Mesoporous Carbon Through Direct Pyrolysis. *Mol. Syst. Des. Eng.* **2023**, *8*, 1156.
- (39) Hunt, M. A.; Saito, T.; Brown, R. H.; Kumbhar, A. S.; Naskar, A. K. Patterned Functional Carbon Fibers from Polyethylene. *Adv. Mater.* **2012**, 24, 2386–2389.
- (40) Yat, S. C.; Berger, A.; Shonnard, D. R. Kinetic Characterization for Dilute Sulfuric Acid Hydrolysis of Timber Varieties and Switchgrass. *Bioresour. Technol.* **2008**, *99*, 3855–3863.
- (41) Robertson, M.; Dunn, C. B.; Qiang, Z. Reaction-induced Morphology Control in Block Copolymers. *Polym. Int.* **2023**, DOI: 10.1002/pi.6562.
- (42) Gordon Cameron, G.; Main, B. R. The Action of Concentrated Sulphuric Acid on Polyethylene and Polypropylene: Part 2—Effects on the Polymer Surface. *Polymer Deg Stab* **1985**, *11*, 9–25.
- (43) Smith, P.; Obando, A. G.; Griffin, A.; Robertson, M.; Bounds, E.; Qiang, Z. Additive Manufacturing of Carbon Using Commodity Polypropylene. *Adv. Mater.* **2023**, *35*, 2208029.
- (44) Robertson, M.; Guillen Obando, A.; Emery, J.; Qiang, Z. Multifunctional Carbon Fibers from Chemical Upcycling of Mask Waste. ACS Omega 2022, 7, 12278–12287.
- (45) Postema, A. R.; De Groot, H.; Pennings, A. J. Amorphous Carbon Fibres from Linear Low Density Polyethylene. *J. Mater. Sci.* **1990**, 25, 4216–4222.
- (46) Penning, J. P.; Lagcher, R.; Pennings, A. J. The Effect of Diamter on the Mechanical Properties of Amorphous Carbon Fibres from Linear Low Density Polyethylene. *Polym. Bull.* **1991**, *25*, 405–412
- (47) Borisov, O. V.; Zhulina, E. B. Effect of Salt on Self-Assembly in Charged Block Copolymer Micelles. *Macromolecules* **2002**, *35*, 4472–4480.

- (48) Lee, A. S.; Bütün, V.; Vamvakaki, M.; Armes, S. P.; Pople, J. A.; Gast, A. P. Electrostatic Control of Block Copolymer Micelles: Charge and Ionic Strength Dependence. *Macromolecules* **2002**, *35*, 8540–8551.
- (49) Sing, C. E.; Zwanikken, J. W.; Olvera De La Cruz, M. Electrostatic Control of Block Copolymer Morphology. *Nat. Mater.* **2014**, *13*, 694–698.
- (50) Matsen, M. W.; Thompson, R. B. Equilibrium Behavior of Symmetric ABA Triblock Copolymer Melts. *J. Chem. Phys.* **1999**, *111*, 7139–7146.
- (51) Hahn, H.; Chakraborty, A. K.; Das, J.; Pople, J. A.; Balsara, N. P. Order-Disorder Transitions in Cross-Linked Block Copolymer Solids. *Macromolecules* **2005**, *38*, 1277–1285.
- (52) Rudolph, T.; Schacher, F. H. Selective Crosslinking or Addressing of Individual Domains within Block Copolymer Nanostructures. *Eur. Polym. J.* **2016**, *80*, 317–331.
- (53) Walther, A.; Göldel, A.; Müller, A. H. E. Controlled Crosslinking of Polybutadiene Containing Block Terpolymer Bulk Structures: A Facile Way towards Complex and Functional Nanostructures. *Polymer* **2008**, *49*, 3217–3227.
- (54) Wang, L.; Hickner, M. A. Low-Temperature Crosslinking of Anion Exchange Membranes. *Polym. Chem.* **2014**, *5*, 2928–2935.
- (55) Lee, G.; Eui Lee, M.; Kim, S. S.; Joh, H. I.; Lee, S. Efficient Upcycling of Polypropylene-Based Waste Disposable Masks into Hard Carbons for Anodes in Sodium Ion Batteries. *J. Ind. Chem. Eng.* **2022**, 105, 268–277.
- (56) Ravikovitch, P. I.; Haller, G. L.; Neimark, A. V. Density Functional Theory Model for Calculating Pore Size Distributions: Pore Structure of Nanoporous Catalysts. *Adv. Colloid Interface Sci.* 1998, 76, 203–226.
- (57) Cychosz, K. A.; Thommes, M. Progress in the Physisorption Characterization of Nanoporous Gas Storage Materials. *Engineering* **2018**, *4*, 559–566.
- (58) Wei, M.; Zhang, L.; Xiong, Y.; Li, J.; Peng, P. Nanopore Structure Characterization for Organic-Rich Shale Using the Non-Local-Density Functional Theory by a Combination of N2 and CO2 Adsorption. *Microporous Mesoporous Mater.* **2016**, 227, 88–94.
- (59) Zhao, D.; Huo, Q.; Feng, J.; Chmelka, B. F.; Stucky, G. D. Nonionic Triblock and Star Diblock Copolymer and Oligomeric Sufactant Syntheses of Highly Ordered, Hydrothermally Stable, Mesoporous Silica Structures. *J. Am. Chem. Soc.* **1998**, *120*, 6024–6036.
- (60) Lv, Y.; Zhang, F.; Dou, Y.; Zhai, Y.; Wang, J.; Liu, H.; Xia, Y.; Tu, B.; Zhao, D. A Comprehensive Study on KOH Activation of Ordered Mesoporous Carbons and Their Supercapacitor Application. *J. Mater. Chem.* **2012**, 22, 93–99.
- (61) Wang, J.; Xue, C.; Lv, Y.; Zhang, F.; Tu, B.; Zhao, D. Kilogram-Scale Synthesis of Ordered Mesoporous Carbons and Their Electrochemical Performance. *Carbon* **2011**, *49*, 4580–4588.
- (62) Stefik, M.; Lee, J.; Wiesner, U. Nanostructured Carbon-Crystalline Titania Composites from Microphase Separation of Poly(Ethylene Oxide-b-Acrylonitrile) and Titania Sols. *Chem. Commun.* **2009**, 2532–2534.
- (63) Fei, H. F.; Long, Y.; Yu, H. J.; Yavitt, B. M.; Fan, W.; Ribbe, A.; Watkins, J. J. Bimodal Mesoporous Carbon Spheres with Small and Ultra-Large Pores Fabricated Using Amphiphilic Brush Block Copolymer Micelle Templates. ACS Appl. Mater. Interfaces 2020, 12, 57322–57329.
- (64) Fei, H. F.; Li, W.; Bhardwaj, A.; Nuguri, S.; Ribbe, A.; Watkins, J. J. Ordered Nanoporous Carbons with Broadly Tunable Pore Size Using Bottlebrush Block Copolymer Templates. *J. Am. Chem. Soc.* **2019**, *141*, 17006–17014.